CrossMark

Determination of the Photometric Calibration and Large-Scale Flatfield of the STEREO *Heliospheric Imagers*: II. HI-2

S.J. Tappin[1] · **C.J. Eyles**[1,2] · **J.A. Davies**[1]

Abstract In this article we describe the methods used to determine the photometric calibration parameters for the outer *Heliospheric Imagers* (HI-2) onboard the *Solar Terrestrial Relations Observatory* (STEREO) spacecraft from measurements of background stars, and we present those values that represent small corrections to the values predicted from pre-launch calibrations. Conversion factors to physical units are also derived. We determine the degradation of these instruments over the course of the mission to date; this is found to be around an order of magnitude slower than for white-light instruments on other spacecraft. We compute a correction to the large-scale flatfield for HI-2A, allowing for vignetting in the outer parts of the images. In addition, we consider the effects of pixel saturation and the implications for the use of the HI-2 instruments for stellar photometry. We also discuss the limitations of the currently employed geometrical projection assumptions.

1. Introduction

The *Solar Terrestrial Relations Observatory* (STEREO: Kaiser *et al.*, 2008), launched in late 2006, is a two-spacecraft NASA mission to investigate the initiation and propagation of coronal mass ejections (CMEs) from locations separated in ecliptic longitude. The two

---

✉ S.J. Tappin
james.tappin@stfc.ac.uk

C.J. Eyles
cje@star.sr.bham.ac.uk

J.A. Davies
jackie.davies@stfc.ac.uk

[1] RAL Space, STFC Rutherford Appleton Laboratory, Chilton, Didcot, Oxon OX11 0QX, UK

[2] Laboratorio de Procesado de Imagenes, Universidad de Valencia, Valencia 46071, Spain

spacecraft were placed in heliocentric orbits, one (the ahead spacecraft; STEREO-A) somewhat inside 1 AU and the other (the behind spacecraft; STEREO-B) somewhat outside. This means the spacecraft drift ahead of and behind the Earth by about 22° per year, and reached solar superior conjunction in early 2015.

The imaging capabilities of STEREO are provided by the *Sun Earth Connection Coronal and Heliospheric Investigation* (SECCHI: Howard *et al.*, 2008), which is a package consisting of an EUV imager, two coronagraphs, and two *Heliospheric Imagers*. The *Heliospheric Imagers* (HI: Eyles *et al.*, 2009) use Thomson-scattered light to detect and track CMEs and other solar-wind disturbances from the outer limits of the coronagraphs to 1 AU and beyond. The HI instruments have a nominally circular field of view offset from the Sun to the earthward side. The inner (HI-1) instruments have a field of view 20° in diameter, centred at an elongation of 14°, while the outer (HI-2) instruments have a field diameter of 70° centred at an elongation of 53°. The photometric calibration and evolution of the HI-1 instruments over the first four STEREO orbits (relative to the background stars) have been described by Bewsher *et al.* (2010) and Bewsher, Brown, and Eyles (2012), respectively.

The present article should be considered as Article 2 to Bewsher *et al.* (2010) (hereafter Article 1), in which the photometric calibration and flatfield of the HI-1 cameras were derived, and also to Bewsher, Brown, and Eyles (2012), which studied the evolution of the HI-1 photometric performance over the STEREO mission. In this article we describe the photometric calibration and large-scale flatfield determinations for the HI-2 instruments. In Section 2 we describe the predicted HI-2 instrument response that has been used until now for calibrating the photometric response of the instruments. In Sections 3 and 4 we describe the photometric calibrations performed in flight using measurements of background stars and present revised photometric calibration parameters based on those analyses. In Section 5 we examine the long-term stability of the instrument responses. In Section 6 we describe in-flight revisions to the large-scale flatfield and related considerations. The appendices provide more details on the handling of stellar magnitudes as applied to the HI-2 instruments, examine the effects of saturation on HI-2 images, and assess the accuracy of assuming the azimuthal perspective projection for HI images.

A note on terminology: since the science images from the HI cameras are 2×2 binned before transmission to Earth (Eyles *et al.*, 2009), it is important to maintain the distinction between pixels on the 2048×2048 camera CCD and pixels in the 1024×1024 science images. Therefore we here refer to a pixel on the CCD as a pixel, and one in a science image as a bin. In general, our analyses are presented in terms of CCD pixels with appropriate conversions to image bins provided.

2. HI-2 Predicted Instrument Response and Pre-launch Flatfield Calibration

Until the analysis that we present in the remainder of this article, the conversion of HI-2 observations to units of mean solar brightness [$B_\odot$] and other units was based on measurements made prior to launch. In this section we describe how these parameters were derived.

2.1. Predicted Instrument Response

The predicted instrument response was derived from a mixture of measurements and manufacturers' data. The contributors to the response are described below.

Figure 1 The optical transmission and quantum efficiencies of the HI-2 instruments. (a) The transmissions and efficiencies displayed separately. Solid = quantum efficiency, dashed = HI-2A, dash–dot = HI-2B. (b) The net effective transmission for the two HI-2 instruments, and also the transmission for HI-1A (dotted) for comparison. The vertical lines show the centroids of the passbands.
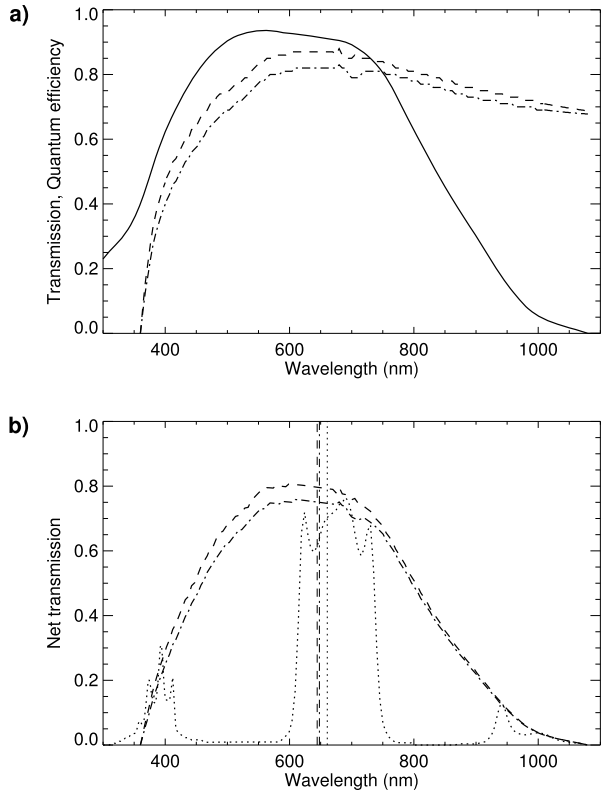
2.1.1. The Transmission of the Optics

Unlike the HI-1 optics, which have a coating to limit the passband, those of HI-2 do not, so the response is broadband. This difference is for a number of reasons; the optics of HI-1 were coated to match the passband to that of the coronagraph COR2 and also to reduce chromatic aberration, but HI-2 was not coated as it was desired to maximise the total light transmission. One consequence of this is that the HI-2 point-spread functions (PSFs) are larger than those of HI-1 partly due to chromatic aberration.

The transmission was determined in three segments: i) Over the wavelength range 400 – 1010 nm, direct measurements of absolute optical transmission obtained during unit-level pre-launch calibration of the HI optics assemblies are used. ii) Above 1010 nm, a simple extrapolation of the measured optical transmission is assumed. iii) Over the range 300 – 400 nm, the transmission of the optics elements is calculated using manufacturers' data for the various glass types used. The transmission is predicted to cut off at approximately 300 nm.

These transmissions are shown as the dashed (HI-2A) and dash–dot (HI-2B) traces in Figure 1a.

2.1.2. The Quantum Efficiency (QE) of the CCD

This is again divided into segments by wavelength. i) Over the range 300 – 1000 nm, the measured values of QE from the CCD manufacturer are used, with a smooth interpolation

between the data points (see Figure 16 of Eyles *et al.*, 2009). ii) Above 1000 nm, a simple extrapolation of the measured QE is assumed where the QE drops to zero at 1080 nm, which is the wavelength corresponding to the band gap in silicon.

The solid trace in Figure 1a shows the resulting efficiency (which is assumed to be identical for all of the HI CCDs). The effective transmission [$T(\lambda)$ in subsequent equations] is then the product of the optical transmission and the QE; this is shown (along with HI-1A for comparison) in Figure 1b.

2.1.3. The Collecting Area

This was derived to be $A = 3.85 \times 10^{-5}$ m^{-2} from the nominal aperture of diameter 7.0 mm (Eyles *et al.*, 2009).

2.1.4. The Camera Gain

The nominal value of $G = 15$ photoelectrons per data number (DN) is used (Eyles *et al.*, 2009).

The integrated counting rate response [DN s^{-1}] to a star whose spectral intensity is $F(\lambda)$ is then given by

$$I_{\text{pred}} = \frac{A}{G} \frac{1}{hc} \int_0^\infty \lambda F(\lambda) T(\lambda) \, d\lambda, \tag{1}$$

where λ is wavelength, h and c are Planck's constant and the speed of light, respectively, and the other terms are as described above.

Until now, the conversion factors used to convert from instrument response in DN s^{-1} (CCD pixel)$^{-1}$ to units of diffuse flux such as B$_\odot$ have been derived from this predicted count rate in the manner described in Section 4.2, using the standard solar reference spectrum of Neckel and Labs (1984).

In later sections of this article, we compare the measured responses to a population of background stars with the responses predicted according to Equation (1) to derive a correction factor to the photometric response:

$$C = \frac{I_{\text{meas}}}{I_{\text{pred}}}. \tag{2}$$

2.2. Pre-launch Flatfield Calibration

Before launch, the large-scale flatfield of the HI-B instruments was calibrated by measuring the response to a calibration light source as a function of its angular position in the field of view (see Eyles *et al.*, 2009). Unfortunately, the test configuration only permitted the calibration source to be scanned along a single axis through the centre line of the field of view. As a result, no information was obtained about any axial asymmetry of the response. Furthermore, due to schedule constraints, it was not possible to perform this calibration on HI-A, which has therefore been assumed to be identical to HI-B.

The response was measured at 1° intervals and was found to be quite accurately represented by a polynomial of the form

$$I = I_0\left(1 + a_1 R^2 + a_2 R^4\right), \tag{3}$$

where R is the radial distance on the detector from the optical axis (assumed to be at the CCD centre) and I_0 is the response on axis. Best-fit numerical values for a_1 and a_2 were
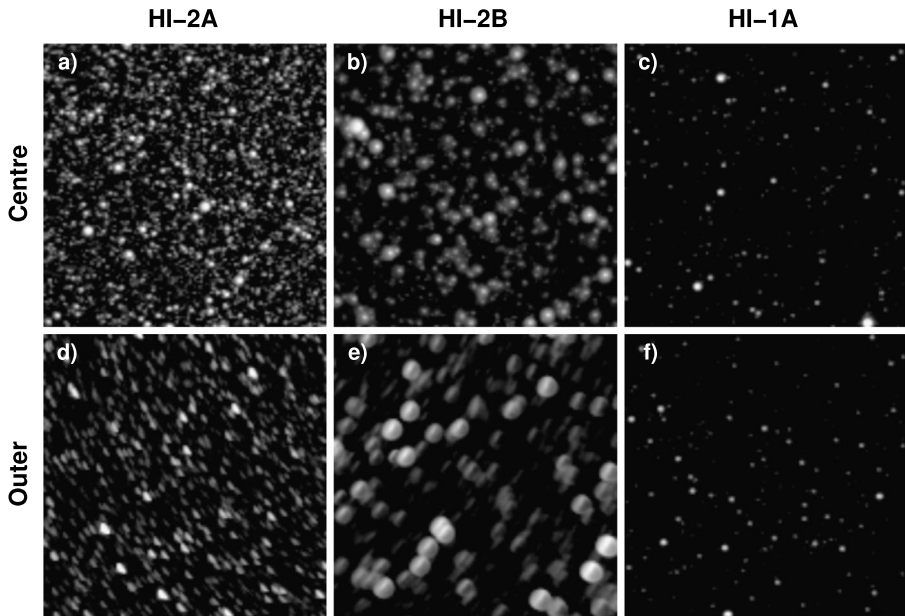
Figure 2 Comparison of the stellar densities and PSFs in the HI-2 fields with those in HI-1. (a, d) HI-2A, (b, e) HI-2B, and (c, f) HI-1A, (a – c) a region at the centre of the field (bins 488:575, 488:575), (d – f) a region in the outer part of the field of view (bins 128:255, 256:383 for HI-2A and HI-1A and 768:895, 256:383 for HI-2B). All are taken from level-2 science images near 1200 UT on 1 September 2011 and are displayed on a logarithmic scale from 0.1 to 20 $\mathrm{DN\,s}^{-1}$ $(\mathrm{CCD\,pixel})^{-1}$.

found to be $a_1 = -6.24 \times 10^{-4}$ mm^{-2} and $a_2 = -1.65 \times 10^{-6}$ mm^{-4} for HI-2B. Before 1 July 2015, this pre-launch flatfield correction was used for processing HI-2 image data, assuming axial symmetry.

3. Photometric Calibration: Method

The methods used in Article 1 to calibrate the HI-1 instruments were not successful when applied to the HI-2 instruments. This is thought to be mainly due to the relatively large PSF of the HI-2 instruments (especially HI-2B) compared with HI-1, and also to the higher density of stars in the images due to the large field of view (Figure 2). For this reason, a new approach to performing stellar photometry has been devised. This method is described in the remainder of this section, and the important differences to the techniques used for HI-1 (Article 1) are explained.

3.1. Defining a Sample

The first step in any calibration using stars is to define a sample of stars with which to perform the calibration.

Since the field of view of HI-2 is large (35° radius), it is not necessary to use very faint stars to obtain a sufficiently large sample. In fact this would be disadvantageous because confusion (the situation where fluctuations in the background from faint stars significantly

influence the measured counting rate for a star Scheuer 1957) will be a problem. For that reason, we have used the "Yale bright star catalogue" (Hoffleit and Warren, 1995) as our source. This provides a list of 9110 stars with, *inter alia*, positions, V magnitudes [m_v], and spectral types down to $m_v = 6.5$, rather than the NOMAD catalogue (Zacharias *et al.*, 2004) used in Article 1.

From this list it is necessary to create a sample suitable for use in calibrating the HI-2 instruments. For that we used the following criteria:

- The object must be a star (although the Yale catalogue is nominally a star catalogue, a few non-stars are listed for historical compatibility).
- It must not be a double (either binary or optical).
- It must not be listed as a variable.
- It must have an ecliptic latitude lower than 35° so that it is actually observed by the HI-2 cameras.
- It must have a HI-2A photonic-magnitude between 2.0 and 5.5. That is to say that the star should have the same expected counting rate in HI-2A (using the pre-launch calibrations) as an A0V star with magnitude between 2.0 and 5.5; see Appendix A for a full explanation of the photonic magnitude. The bright limit of 2.0 was chosen because stars brighter than this show significant smearing in the CCD column direction due to saturation effects. The faint limit was chosen to give an acceptable number of stars while minimising the contributions of confusion. Near the field centre, using the star counts given by Allen (1976) and the typical stellar areas that we found in the course of this analysis, this threshold is about 25 times the brightness of stars with a density of one per PSF at low galactic latitude in HI-2A and 13 times for HI-2B. We used the HI-2A values for convenience as the differences between HI-2A and HI-2B magnitudes are small.
- It must have a spectral type that can be matched to a spectrum in Pickles' collection of stellar spectra (Pickles, 1998). A spectral match is considered valid if the luminosity class is a single value and the spectrum is not flagged as variable or peculiar, and one of the following is satisfied:

  i) There is an exact match to a type with a spectrum.
  ii) The spectral type lies within a range that shares a common spectrum in Pickles' catalogue.
  iii) The spectral type is a range that spans a spectrum in Pickles.
  iv) The spectral type can be matched by interpolating between two spectra separated by no more than three subclasses (*e.g.* K4 could be derived from K2 and K5, but not from K2 and K6).

In all cases an exact luminosity class match is required (*e.g.* we would not attempt to interpolate between A2I and A2III to obtain a spectrum for A2II). Unlike the HI-1 analysis in Article 1, it was not necessary to resort to colour mixing as we had spectral types for all of the stars in our sample and the vast majority could be matched to spectra in Pickles (1998); those few that could not be matched were discarded. Indeed, it is uncertain whether colour mixing could be effectively applied to the much broader passband of HI-2.

By applying the criteria above, we arrive at a sample of 575 stars that are potentially useful for calibrating the HI-2 instruments. The characteristics of these stars are available in the supplementary file star_list_all.csv (the contents of the columns are described in the file README).

For each star in the sample, a predicted count rate was determined for each of the HI-2 instruments by integrating the product of the spectrum and the passband over wavelength

and applying the calibration parameters described in Section 2. The details of the spectral calibration and integration are described in Appendix A.

3.2. Measuring Stellar Brightness

Determining the total counting rate of a star in the HI-2 instruments is the main problem that has held up the production of a post-launch calibration of the HI-2 instruments. Whilst the absence of such a photometric calibration has not hindered the analysis of numerous solar transients and the publication of many results, it is clear that a robust calibration will pave the way to many additional lines of research.

   To avoid unnecessary duplication of processing, we chose to use the Level-2 science data images in instrument units ($DN s^{-1} (CCD pixel)^{-1}$) with a three-day background subtracted to remove the stable background (mainly the F-corona). The details of the processing are summarised on the UK Solar System Data Centre (UKSSDC) web site (www.ukssdc.ac.uk/solar/stereo/documentation/HI_processing.html and www.ukssdc.ac.uk/solar/stereo/documentation/HI_processing_L2_data.html). In summary: the raw images are converted from units of DN to units of $DN s^{-1} (CCD pixel)^{-1}$, the readout smearing caused by the shutterless cameras (Eyles *et al.*, 2009) is removed, severely saturated bins are flagged, the pre-launch large-scale flatfield is applied, and a three-day running mean of the lowest quartile of the measurements for each individual bin is subtracted.

   The aperture-photometry method employed for HI-1 of defining an inner disk for the star and an outer ring for the background (Article 1) was found to give inconsistent results for HI-2. Preliminary analysis suggests that when the inner disk is large enough to not miss a significant fraction of the stellar flux, then the outer ring becomes large enough that there are problems with confusion. It was therefore necessary to devise a new method for defining a star and the surrounding background level. After some experimentation, the following procedure was found to work for the vast majority of stars and to give fluctuations in measured count rate that were lower than 3 % over short (one-day) time scales. Examples of a number of the stages of the procedure are shown in Figure 3, for both HI-2A (panels a – e) and HI-2B (panels f – j):

   i) Start at the calculated star position (using its catalogue position and the SolarSoft WCS routines (Thompson and Wei, 2010) with the projection parameters derived by Brown, Bewsher, and Eyles 2009).

  ii) Select a region surrounding that position within which all subsequent analysis will be done. For HI-2A we used a 25×25 bin region (this is about 1.8° square at the centre of the CCD), while for HI-2B we used a 31×31 region (about 2.2° at CCD centre). These sizes were chosen to be large enough to allow a reasonable region of background around the star even in the outer parts of the field of view where the PSFs are larger, but also small enough that there should not be major effects on the background from gradients such as the galactic plane (Figure 3a, f).

 iii) Locate the nearest bin to the calculated stellar position that is a maximum using a simple gradient-following method. Except near the edge of the field of view, this is almost always the bin containing the calculated position. This is marked by a + symbol in Figure 3a, f.

  iv) Define a "high-flux" region as those contiguous bins surrounding the peak that have values at least one-third of the peak value. This area is considered to always be part of the star image (Figure 3b, g).

   v) Define a new central location as the centroid of the "high-flux" region. This gives a better measure of the centre than the peak bin as some PSFs (particularly in the outer
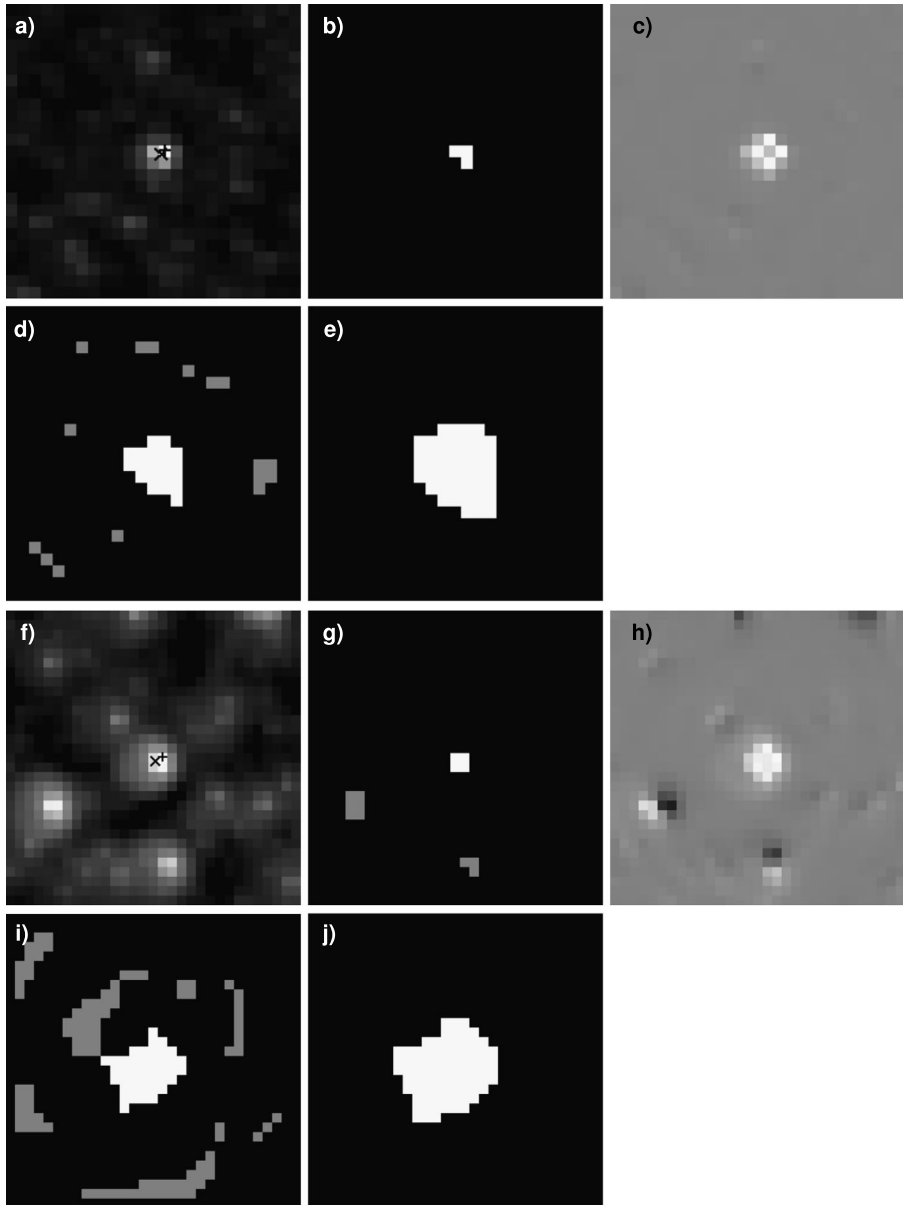
Figure 3 Illustration of the star-region definition algorithm in action. (a–e) HI-2A, (f–j) HI-2B. (a, f) The region to be analysed, scaled using a square-root scaling to allow the lower-level structure to be seen. The +-sign indicates the peak pixel and the ×-sign the centroid of the high region. (b, g) The high-level regions, with the region for the star in white, other high areas in grey. (c, h) The radial gradient (white is negative). (d, i) The union of the high region and the negative gradient region (grey indicates those regions not encompassing the star centre). (e, j) The region defined to be part of the star. Both sequences come from images starting at 12:09:21 UT on 1 September 2011. The star in HI-2A is Yale 8093, HD201381, νAqu, a G8III star of $m_v = 4.51$, while that in HI-2B is Yale 307, HD6386, 73Psc, a K5III star of $m_v = 6.00$. The HI-2A fields are about $1.8°$ square, and those for HI-2B are about $2.2°$ square.
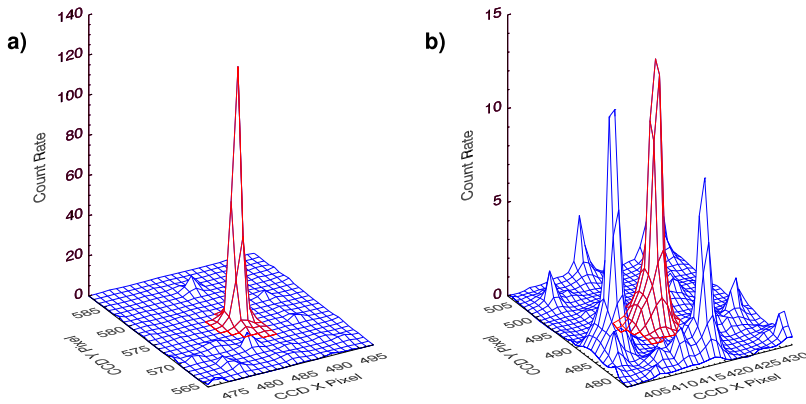
Figure 4 Examples of the bin selection for star images. (a) HI-2A and (b) HI-2B. The region indicated in red is that determined to be part of the star image, while the blue is the background region. As in Figure 3, both fields come from images starting at 12:09:21 UT on 1 September 2011. The star in HI-2A is Yale 8093, HD201381, νAqu, a G8III star of $m_v = 4.51$, while that in HI-2B is Yale 307, HD6386, 73Psc, a K5III star of $m_v = 6.00$. The HI-2A fields are about $1.8°$ square, and those for HI-2B are about $2.2°$ square.

parts of HI-2B) have two peaks, or are strongly asymmetrical. This is again rarely more than a few tenths of a bin away from the calculated position. This is marked by a $\times$-symbol in Figure 3a, f.

vi) Compute the gradient of the portion of the image in the analysis region using numerical differentiation, with a three-point Lagrangian interpolation (IDL routine DERIV); from that, compute the radial gradient of the image away from this new central location (Figure 3c, h).

vii) Mark bins with negative gradient, and then apply the morphological ERODE operator (Gonzalez and Woods, 2008) with a 3×3 kernel to remove pixels from the edge of the marked regions to separate zones.

viii) Take the union of the "high-flux" region and the negative gradient regions (Figure 3d, i).

ix) Label the resulting map into contiguous regions, and only select the region including the peak.

x) Apply the morphological DILATE operator (Gonzalez and Woods, 2008) to this region to reverse the effect of the earlier ERODE (Figure 3e, j).

The regions defined by the sequences in Figure 3 are shown as surface plots in Figure 4; the HI-2B example is quite close to the limit of brightness *vs.* starfield density at which the method will work effectively.

The background level is taken to be the median of all of the bins in the analysis region that are not in the star image. The total counting rate of the star is taken to be four times the sum of all the bins in the star image region after the background level has been subtracted. The use of a median background level determined over a relatively large area ensures that i) the background level will not be affected by nearby bright stars, ii) the contribution of stars below the confusion limit is handled in an unbiased way, and iii) an excessively crowded starfield will be flagged by an abnormally high background. The factor of four is required as the counting rates are in units of $DN\,s^{-1}\,(CCD\,pixel)^{-1}$, but we are summing over bins rather than pixels.

For each science image from the start of STEREO science operations in March 2007 up to the end of 2013, we used the method described above to measure a counting rate for

each of the stars from our sample that fell in the nominal 512-bin radius field of view of the instrument. Although stars can be seen in the corners of the CCD, they are heavily vignetted and distorted beyond the nominal field of view.

3.3. The Correction Factor

To determine the correction factors of the measured instrument responses relative to the predicted response (Section 2), we used only values from stars whose calculated position was within 100 bins of the centre of the field of view. This was chosen as it is considered unlikely that there are significant deviations of the flatfield from pre-launch values within that region; this assumption has been confirmed *a postiori* by the flatfield analysis presented in Section 6.

To exclude "poorly behaved" and ill-characterised stars, we found it necessary to apply a number of additional selection criteria; these were mainly empirically determined thresholds selected to remove the problematic stars without eliminating too many useful ones:

- The median summed count rate of the star must not exceed 2000 DN s^{-1}, as it is found that above this threshold there is a clear turn down of the observed relative to the predicted rates that is due to saturation of the highest pixels in the stellar image (see Appendix B for further discussion of this issue).
- Neither the interquartile range of the individual count rates of the star nor their standard deviation excluding points below the 5th and above the 95th percentile may exceed 4 % of the median count rate. This is to exclude stars that blend with others in part of their track across the field of view.
- There must not be another bright star (*i.e.* any star in the Yale list) within 0.5° of the star.
- In the preliminary flatfield analyses (Section 6), the star must not have had a minimum count rate more than 20 % above the fitted trend, nor a maximum rate more than 20 % below the trend.
- Stars that showed obvious discontinuities in their count rate tracking across the central region of the field were also excluded manually.
- The median of the background (*i.e.* the background level as described above multiplied by the number of bins in the stellar image) must not exceed 8 % of the star's median counting rate for HI-2A, or 15 % for HI-2B. This is mainly a precaution against false backgrounds in crowded fields.
- There must be at least 50 measurements of the star; this excludes some stars that passed through the HI-2B field when the spacecraft roll relative to the ecliptic plane was large early in the mission (the STEREO-A roll was already small by the start of the HI science observations).

There is in fact a very considerable overlap between these criteria, *i.e.* most of the stars excluded fail on more than one of the thresholds.

This left a total of 62 stars for HI-2A and 54 for HI-2B (out of 113 and 127, respectively, that pass through the 100-bin region) that could be used for the photometric calibrations. While this is many fewer than were used for HI-1 in Article 1, it is comparable with the number used in the calibrations of the *Large Angle and Spectrometric Coronagraph* (LASCO) C3 coronagraph onboard the *Solar and Heliospheric Observatory* (SOHO) (Thernisien *et al.*, 2006). The stars used are marked by an "A" or "B" in the "Used" column of the supplementary file star_list_all.csv.

We then took the median count rates for all stars that satisfied the above criteria and fitted a linear trend constrained to pass through the origin, using a weighted L1 norm (least absolute residual) fit. Each input value was weighted by N_{obs}/IQ, where N_{obs} is the number of
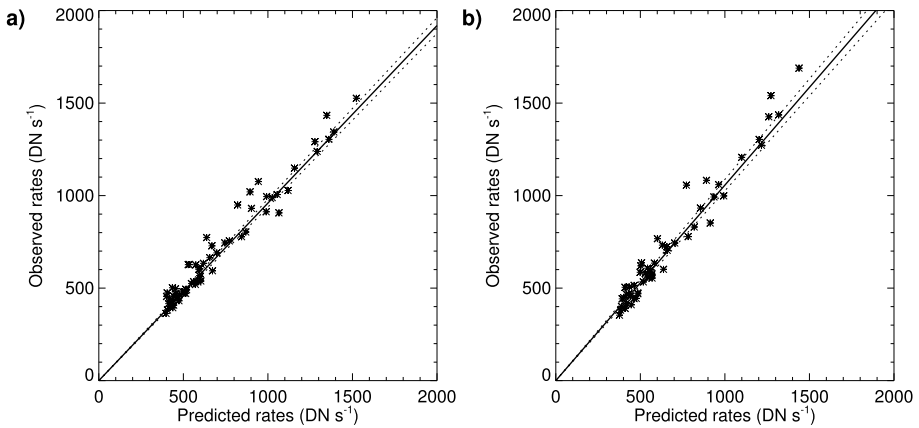
Figure 5 Correlations between the observed and predicted count rates for the core-region stars: (a) HI-2A and (b) HI-2B. The solid lines indicate the best fits, and the dotted lines show the estimated 1σ limits.

measurements for the star and was typically between 800 and 900, and *IQ* is the interquartile range for the observations of that star. The L1 norm was chosen because the underlying distribution is unknown, which means that parametric techniques are not appropriate (*e.g.* Wall 1979, 1996, Branham 1982). It also became clear from the orbit-by-orbit analysis (Section 5) that the deviations of each star from the trend are dominated by systematic effects. The estimation of errors for L1-norm fitting is not a precise science, but if we *assume* that the errors are equally likely to be positive or negative, then the 1σ limit can be approximated by the $\frac{1}{2} \pm \frac{1}{\sqrt{N_s}}$ quantile fits (Koenker and Hallock, 2001), where N_s is the number of stars used. We also note that the results obtained from L2-norm (least-squares) fitting are not significantly different from those presented here.

In addition to the main fitting, we also carried out consistency checks by dividing the core region into five sub-regions (an inner 50-bin radius circle and four outer quadrants running from 50 to 100 bins) and carrying out similar fits for each of these regions.

To at least crudely check the shape of the spectral response, we also compared the results when the stars were split into three broad spectral groups: early type (B1 to G5), intermediate type (G6 to K3), and late type (K4 to M3). These limits were chosen to give roughly equal numbers of stars in each category.

4. Photometric Calibration: Results

4.1. Scaling Factors

The correlation results are shown in Figures 5 and 6, and they are summarised in Table 1.

It is clear then that the correction factors are very consistent, with none of the sub-category fits differing from the global fit by more than about 1σ. It should be noted that the difference between HI-2A and HI-2B is greater than the difference in the values predicted from the pre-launch calibrations, and in the opposite sense, meaning that HI-2B is actually the *more* sensitive instrument. We cannot determine whether the differences from the predicted values are due to differences in the optical transmission, the CCD efficiency, uncertainties in the effective aperture size, or the analogue-to-digital converter gain.
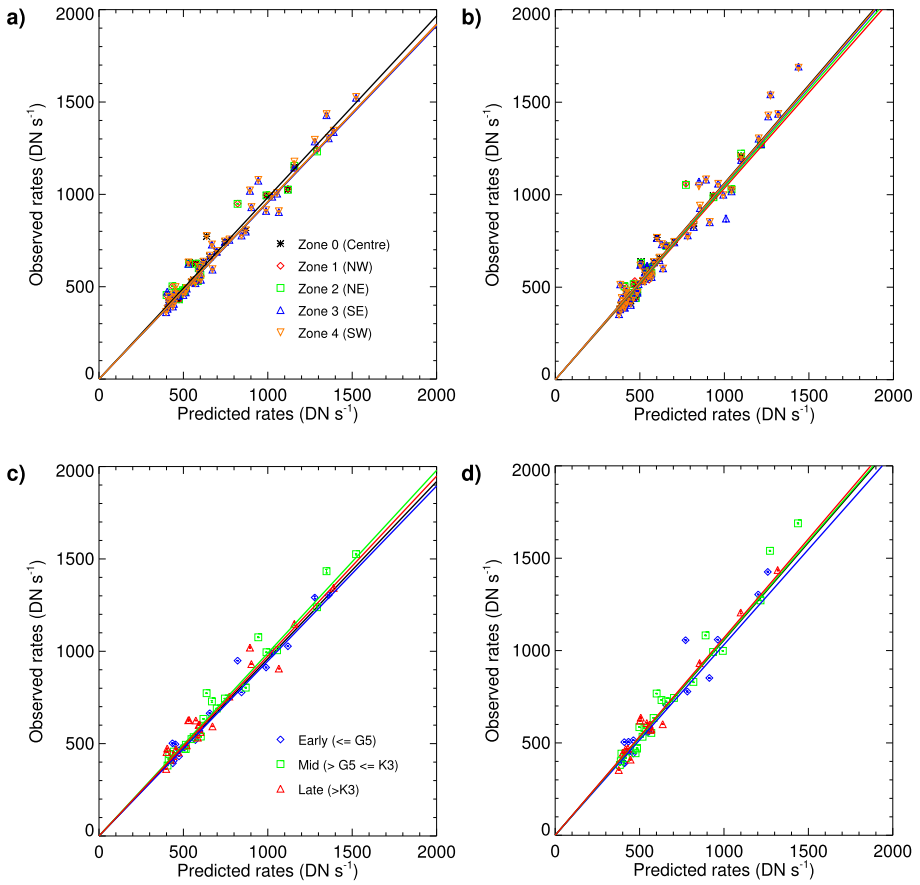
Figure 6 Correlations between observed and predicted count rates for the various sub-samples used. (a) HI-2A by zone, (b) HI-2B by zone, (c) HI-2A by spectral type, and (d) HI-2B by spectral type. In panels c and d, the black line is the corresponding fit from Figure 5.

Table 1 Fitted calibration corrections for the core region.

Fit to:	HI-2A			HI-2B		
	Value	Error	N_s	Value	Error	N_s
All	0.959	0.02	62	1.057	0.03	54
Zone 0	0.983	0.03	23	1.062	0.05	24
Zone 1	0.961	0.04	19	1.035	0.05	17
Zone 2	0.959	0.05	19	1.045	0.04	17
Zone 3	0.956	0.03	43	1.055	0.04	49
Zone 4	0.959	0.03	44	1.059	0.04	45
B1-G5	0.947	0.02	18	1.032	0.05	16
G6-K3	0.990	0.03	22	1.061	0.06	15
K4-M3	0.974	0.02	22	1.070	0.09	23

Table 2 Conversion factors from $\mathrm{DN\,s^{-1}\,(CCD\,pixel)^{-1}}$ to physical units for HI-2A and HI-2B.

To convert images in $\mathrm{DN\,s^{-1}}$ $(\mathrm{image\,bin})^{-1}$, these numbers must be divided by 4.

Unit	HI-2A	HI-2B
$B_\odot$	4.437×10^{-14}	4.306×10^{-14}
S10	98.62	95.72
$\mathrm{W\,m^{-2}\,sr^{-1}}$ $(0-\infty)$	8.873×10^{-7}	8.612×10^{-7}
$\mathrm{W\,m^{-2}\,sr^{-1}}$ $(360-1080\ \mathrm{nm})$	6.163×10^{-7}	5.982×10^{-7}
$\mathrm{W\,m^{-2}\,sr^{-1}}$ (passband)	3.154×10^{-7}	3.149×10^{-7}

4.2. Conversion to Physical Units

The calibrations presented above relate to the response of the HI-2 instruments to point sources. To be useful for the primary purpose of the instruments within the STEREO mission, we must relate these values to useful quantities for diffuse sources. Here we follow the methods used in the HI-1 calibrations (Article 1), except that we also provide some additional SI unit conversions. Numerical values of all the conversion factors are presented in Table 2, and their derivation is discussed below.

4.2.1. The On-axis Conversion Factors

The primary target of the heliospheric imagers is Thomson-scattered light from the solar wind, which preserves the source spectrum; it is therefore appropriate to consider only solar-type spectra. In addition, since the science images supplied by the UKSSDC are averaged over the 2×2 binning, rather than summed, the appropriate unit for the conversion factors is from $\mathrm{DN\,s^{-1}\,(CCD\,pixel)^{-1}}$ rather than from $\mathrm{DN\,s^{-1}\,(image\,bin)^{-1}}$. It should also be noted here that since the surface brightness of an extended source is independent of the viewing distance, we do not need to adjust the scaling factors for the orbital distance of the spacecraft; however, we do need to be consistent in the distance at which extensive quantities are measured. Tabulations such as those of Allen (1976) are for observers at 1 AU, therefore we use 1 AU values in this analysis.

The traditional unit for coronagraph and heliospheric imager data is the mean solar brightness ($B_\odot$), which is the average surface brightness of the solar disk. The scaling factor may be defined as

$$C(B_\odot) = \frac{n_{\mathrm{pix}}}{I_\odot}, \tag{4}$$

where n_{pix} is the number of pixels covered by the solar image, and $I_\odot$ is the computed total counting rate for the Sun in $\mathrm{DN\,s^{-1}}$.

$$n_{\mathrm{pix}} = \pi \left(\frac{\Theta_\odot}{D_{\mathrm{pix}}} \right)^2, \tag{5}$$

where $\Theta_\odot$ is the angular radius of the Sun, taken to be 960 arcsec (Allen, 1976), and D_{pix} is the angular size of a CCD pixel at the centre of the field of view (130.03 arcsec for HI-2A and 129.80 arcsec for HI-2B, Brown, Bewsher, and Eyles 2009).

$$I_\odot = \frac{A}{G} \frac{1}{hc} \int_0^\infty \lambda F_\odot(\lambda) T(\lambda) \, d\lambda. \tag{6}$$

This is the same as Equation (1), with the solar spectral power $F_\odot(\lambda)$ in place of a generic stellar spectrum. The results presented here were derived using $F_\odot(\lambda)$ from the solar spectrum published by Neckel and Labs (1984), which was also used in Article 1. In addition,

we repeated the computations using two other spectra: firstly the higher resolution spectrum from Kurucz *et al.* (1984), and secondly the generic G2V spectrum given by Pickles (1998). The Kurucz *et al.* spectrum gave conversion factors about 2.3 % larger than using the Neckel and Labs spectrum, while those using the generic spectrum from Pickles were about 0.5 % smaller.

The S10 unit is defined to be a surface brightness equivalent to one $m_v = 10.00$ solar-type star per square degree. This is related to the counting rate by

$$C(S10) = \frac{1}{I_{10}\Omega_{\text{deg}}}, \tag{7}$$

where I_{10} is the computed integrated count rate for a magnitude 10 solar-type star and $\Omega_{\text{deg}} = D_{\text{pix}}^2$ is the solid angle subtended by a pixel in square degrees. I_{10} is easily computed from $I_\odot$ using the known visual magnitude of the Sun $m_{v\odot} = -26.74$ (Allen, 1976) as $I_{10} = I_\odot \times 10^{-36.74/2.5}$.

To convert to SI units of $\mathrm{W\,m^{-2}\,sr^{-1}}$, we use the relation

$$C(\text{SI}) = \frac{P}{I_\odot \Omega_{\text{pix}}}, \tag{8}$$

where $\Omega_{\text{pix}} = \Omega_{\text{deg}}(\frac{\pi}{180})^2$ is the solid angle subtended by a pixel in steradians. P is the power in the solar spectrum, which can usefully be determined in at least three ways:

 i) The total power across all wavelengths: $P = \int_0^\infty F_\odot(\lambda)\,d\lambda$. (*i.e.* the solar constant of 1361 $\mathrm{W\,m^{-2}}$; Kopp and Lean 2011).
 ii) The total power in the wavelength range to which the HI-2 detectors are sensitive, 360 to 1080 nm: $P = \int_{360}^{1080} F_\odot(\lambda)\,d\lambda$. (945 $\mathrm{W\,m^{-2}}$).
iii) The total power detected by the HI-2 detectors: $P = \int_0^\infty F_\odot(\lambda)T(\lambda)\,d\lambda$. (487 $\mathrm{W\,m^{-2}}$ for HI-2A, 513 $\mathrm{W\,m^{-2}}$ for HI-2B).

These updated calibration parameters along with the time-dependency described in Section 5 were added to versions of secchi_prep after 1 July 2015.

4.2.2. *Geometrical Correction for Extended Sources*

The values quoted above are derived using the pixel solid angle on the optical axis. For extended sources, it is also necessary to consider the variation of pixel solid angle across the field of view. The relation for this correction, which was provided in the unnumbered relation following Equation (18) in Article 1, is oversimplified (essentially it assumes that each pixel views a square region of the sky), therefore we present a more rigorous version here.

As discussed by Brown, Bewsher, and Eyles (2009), the projection of the HI instruments can be well-approximated by the azimuthal-perspective projection (AZP: Calabretta and Greisen, 2002), and in this section we use this. It should be emphasised here (as it was by Brown, Bewsher, and Eyles 2009) that the optics design of the HIs has no relationship to the geometrical construction of the AZP projection, but that the link is merely an empirical one, in that it was found to give a good fit to the observed behaviour of the optics. The AZP projection is characterised by the relation

$$R = \frac{F_p(\mu + 1)\sin\alpha}{\mu + \cos\alpha}, \tag{9}$$

Figure 7 The variation of the diffuse correction factor [ρ] across the HI-2 CCDs: HI-2A is the solid line, HI-2B is the dashed line. The vertical dotted line indicates the edge of the nominal field of view.
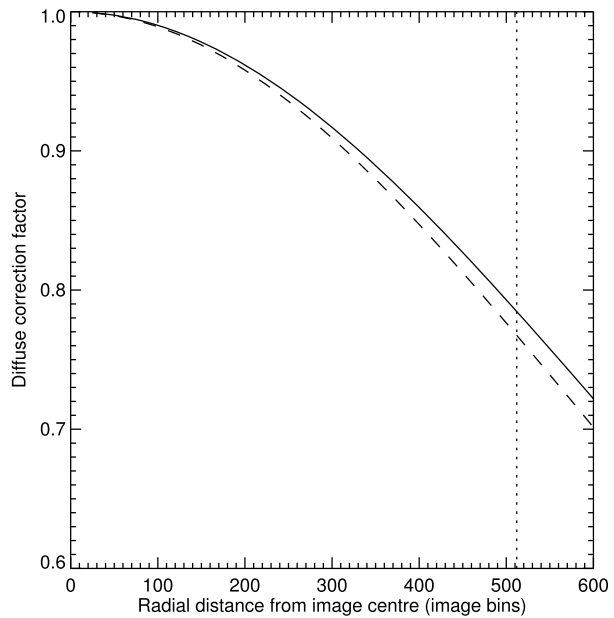
where R is the radial distance on the detector from the optical axis, α is the angular distance of the source from the optical axis, F_p is the paraxial focal length, and μ is a distortion parameter.

From this relation we can derive an expression for the factor [ρ] by which the raw image must be divided to correct for the pixel solid angle as

$$\rho = \frac{\delta\Omega(\alpha)}{\delta\Omega(0)} = \frac{(\mu + \cos\alpha)^3}{(\mu+1)^2(\mu\cos\alpha + 1)}, \tag{10}$$

where $\delta\Omega(\alpha)$ is the solid angle of the pixel (or bin) at an angle α from the CCD centre. This may then be related to the physical distance from the CCD centre using Equation (19):

$$\cos\alpha = \frac{-\mu + \gamma\sqrt{1 - \mu^2 + \gamma^2}}{1 + \gamma^2},$$

where, $\gamma = F_p(\mu + 1)/R$. The resulting variation of ρ across the HI-2 fields of view is shown in Figure 7. The details of the derivation are presented in Appendix C.

An investigation of the accuracy of the AZP projection when applied to the HI-2 instruments is presented in Appendix D.

This relation for ρ is used in current versions of the secchi_prep routine distributed in SolarSoft and has been used in the physical-unit images distributed from the UKSSDC.

5. Evolution of the Sensitivity

The analyses and results presented in Sections 3 and 4 assume that the properties of the instrument do not change with time. It is well known, however, that the sensitivity of most space-based detectors degrades with time (*e.g.* Thernisien *et al.* 2006, Buffington *et al.* 2007, BenMoussa *et al.* 2013).
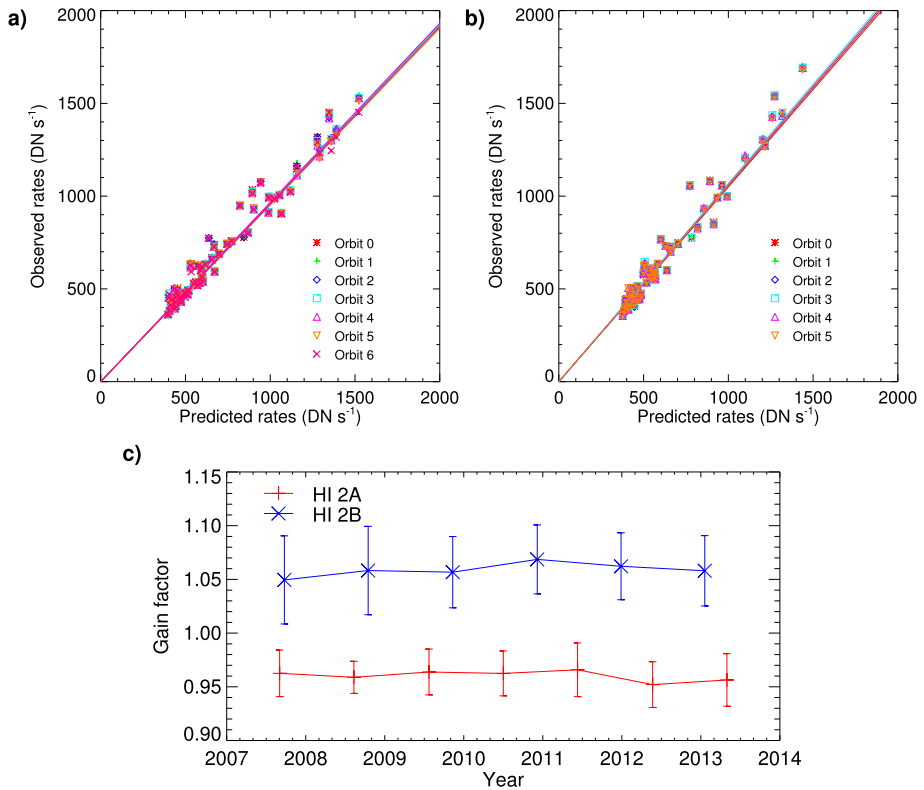
Figure 8 Correlations of counting rates for (a) HI-2A and (b) HI-2B subdivided by STEREO orbit. (c) The evolution of the fitted slopes, red = HI-2A and blue = HI-2B. Note that in most cases the star values for earlier orbits in (a) and (b) are obscured by those from later orbits.

To test for any degradation of the sensitivity of the HI-2 instruments through the mission, we divided the observations by STEREO orbit (seven orbits for HI-2A and six for HI-2B) and carried out a similar analysis to that described in Section 3 on each orbit. These results are shown in Figure 8 and the upper part of Table 3. From these results it is not possible to see any degradation over the course of the mission at about the 1 % level. However, because it is clear from Figure 8 that the individual stars show far less variation from orbit to orbit than their deviations from the general trend suggests that we can improve our sensitivity to potential gain degradation by adjusting each star's count rate by its fractional deviation from the trend in the whole-mission fit (Figure 5).

When these adjustments are applied, we obtain a much better-constrained result, as seen in Figure 9 and the lower part of Table 3. If we fit a straight line to these trends, we obtain $S(T) = 1.0058 - 0.0016\,T$ for HI-2A and $S(T) = 1.0031 - 0.0007\,T$ for HI-2B, where T is the time in years after 2007.0 and $S(T)$ is the sensitivity relative to the mission-to-date values in the first row of Table 1. These correspond to a degradation of 0.16 % year^{-1} for HI-2A and 0.07 % year^{-1} for HI-2B. This result shows that the degradation of the HI-2 detectors and optics is small over a period of more than six years.

This measurement is considerably smaller than the upper limit of about 1 % per year found for HI-1 by Bewsher, Brown, and Eyles (2012) and by BenMoussa *et al.* (2013). The degradation rate for the HI-2 cameras is almost an order of magnitude lower than has been

Table 3 Fitted correction factors by STEREO orbit. Upper rows: fitting to the raw count rates, lower rows: fitting to the adjusted count rates.

Orbit	HI-2A				HI-2B			
	Start	Value	Error	N_s	Start	Value	Error	N_s
Fitting to the raw count rates								
1	14 Mar. 2007	0.963	0.02	58	14 Mar. 2007	1.050	0.04	39
2	21 Feb. 2008	0.959	0.01	58	05 Apr. 2008	1.058	0.04	50
3	31 Jan. 2009	0.964	0.02	60	29 Apr. 2009	1.057	0.03	51
4	10 Jan. 2010	0.962	0.02	59	23 May 2010	1.069	0.03	52
5	21 Dec. 2010	0.966	0.03	59	17 Jun. 2011	1.062	0.03	51
6	30 Nov. 2011	0.952	0.02	58	10 July 2012	1.058	0.03	52
7	09 Nov. 2012	0.956	0.02	60	03 Aug. 2013			
	19 Oct. 2013							
Fitting to the adjusted count rates								
1	14 Mar. 2007	1.0018	0.0005	58	14 Mar. 2007	1.0026	0.0007	39
2	21 Feb. 2008	1.0032	0.0006	58	05 Apr. 2008	1.0017	0.0006	50
3	31 Jan. 2009	1.0030	0.0006	60	29 Apr. 2009	1.0013	0.0009	51
4	10 Jan. 2010	1.0021	0.0009	59	23 May 2010	1.0007	0.0005	52
5	21 Dec. 2010	1.0006	0.0005	59	17 Jun. 2011	1.0000	0.0007	51
6	30 Nov. 2011	0.9973	0.0008	58	10 July 2012	0.9976	0.0008	52
7	09 Nov. 2012	0.9954	0.0010	60	03 Aug. 2013			
	19 Oct. 2013							

found for the white-light coronagraphs onboard the SOHO mission, where Thernisien *et al.* (2006) found a decrease of sensitivity of the LASCO-C3 instrument by 3.5 % over eight years of operation, whilst Llebaria, Lamy, and Danjard (2006) reported a degradation of the LASCO-C2 instrument by 0.7 % per year. For the *Solar Mass Ejection Imager* (SMEI) onboard the Coriolis mission, Buffington *et al.* (2007) found a 1.6 % per year decline of sensitivity, again an order of magnitude worse than HI-2A. While we do not have a definitive explanation of the better durability of the HI-2 cameras compared with LASCO and SMEI, we suspect that improvements in CCD technology since the building of SOHO and the stable thermal and radiation environments of STEREO (*cf.* SMEI) are major factors.

The degradation rates can be converted to yield time-dependent forms for the physical conversion factors given in Table 2; these are given in Table 4. The changes over the course of the mission-to-date are of the same order as the uncertainty in the absolute calibration, but the trend is clear and relevant to relative photometry, and we also expect the trend to continue into the future. For that reason, we have included the degradation in the $B_\odot$ and S_{10} conversions in `secchi_prep` since 1 July 2015. The evolution of the sensitivity will continue to be monitored after the end of the solar-conjunction phase of the mission.

6. Flatfield Determination

In addition to determining the gain corrections at the centre of the HI-2 fields, we also examined the variation of gain across the field of view. The large-scale flatfield is the variation of effective gain caused by, *inter alia*, the change in effective aperture as a function of entry angle and vignetting and differing optical paths within the instrument optics, as well as
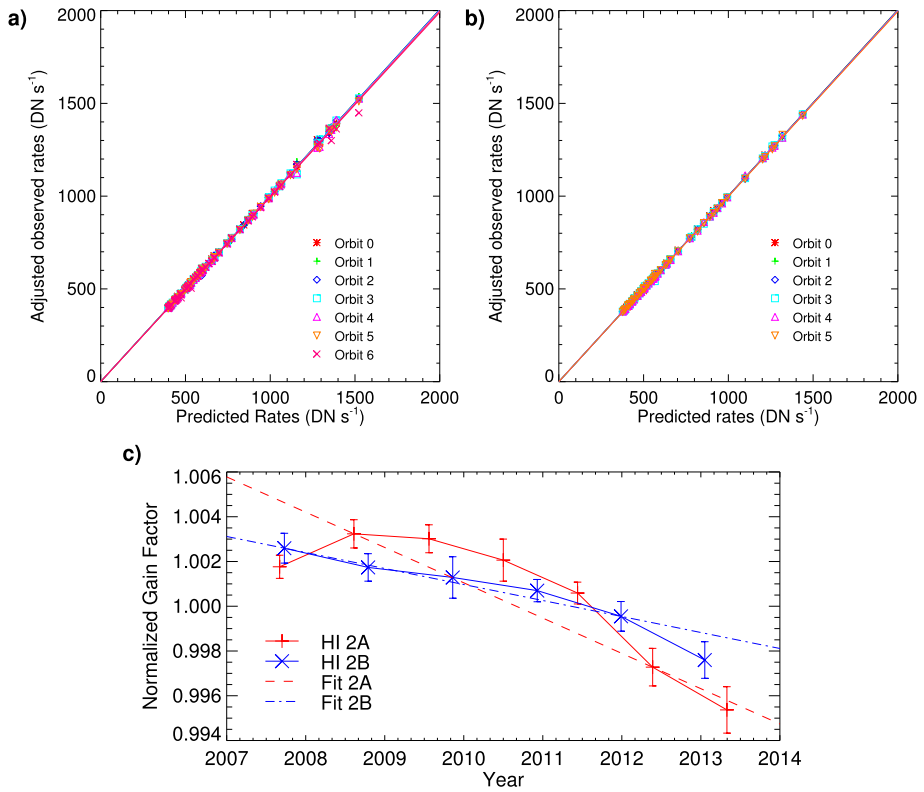
Figure 9 Adjusted counting rate correlations by STEREO orbit and the resulting trends: (a) HI-2A and (b) HI-2B subdivided by STEREO orbit. (c) The evolution of the fitted slopes, red = HI-2A and blue = HI-2B. Note that in most cases the star values for earlier orbits in (a) and (b) are obscured by those from later orbits. The dashed and dash–dot lines in (c) are the best-fit linear trends.

Table 4 Time-dependent conversion factors from $DN\,s^{-1}\,(CCD\,pixel)^{-1}$ to physical units for the HI-2 cameras.

Unit	HI-2A		HI-2B	
	2007.0	per year	2007.0	per year
$B_\odot$	4.411×10^{-14}	7.099×10^{-17}	4.293×10^{-14}	3.014×10^{-17}
S10	98.051	0.158	95.424	0.067
$W\,m^{-2}\,sr^{-1}$ $(0-\infty)$	8.822×10^{-07}	1.420×10^{-09}	8.585×10^{-07}	6.028×10^{-10}
$W\,m^{-2}\,sr^{-1}$ $(360-1080\,nm)$	6.127×10^{-07}	9.861×10^{-10}	5.964×10^{-07}	4.187×10^{-10}
$W\,m^{-2}\,sr^{-1}$ (passband)	3.136×10^{-07}	5.046×10^{-10}	3.139×10^{-07}	2.204×10^{-10}

any large-scale variations in CCD sensitivity. This is separate from, and independent of, the pixel-solid-angle corrections described above, and it affects stellar measurements as well as diffuse sources.

The first approach was to divide the whole field of view into a number of sub-regions and follow the approach described in Section 4.1 to determine gain corrections for each

Table 5 Fitted large-scale flatfield parameters for HI-2.

	Bins	Pixels	mm
HI-2B, pre-launch			
a_0	1.0	1.0	1.0
a_1	-1.59×10^{-7}	-3.98×10^{-8}	-2.18×10^{-4}
a_2	-8.77×10^{-13}	-5.48×10^{-14}	-1.65×10^{-6}
HI-2A, in-flight			
a_0	1.045	1.045	1.045
a_1	-6.417×10^{-7}	-1.604×10^{-7}	-8.802×10^{-4}
a_2	-7.317×10^{-14}	-4.573×10^{-15}	-1.377×10^{-7}
a_3	-2.254×10^{-5}	-5.635×10^{-6}	-0.0309
a_4	448.8	897.6	12.12

sub-region. Initial versions of this approach were dominated by striations parallel to the x-axis (*i.e.* tracking the motion of stars across the CCD). When the causes of this were analysed, we found that a number of stars were consistently high or low (mostly high) relative to the fitted trend. This probably is most commonly caused by cases where the star region identification includes another star (which would occur if the saddle point between the stellar responses was above one-third of the peak of one of the stars). For this reason, we created a blacklist of stars for each instrument that contained those stars whose lowest value in any of the boxes was more than 20 % above the fitted trend or whose highest value was more than 20 % below the trend. These lists were also fed back into the photometric calibration analysis.

After this modification, the star-track aligned striations were much reduced relative to the original version, but they still dominated the maps. It was clear, however, that the main systematic deviation was a fall-off of sensitivity towards the edge of the field.

The effect of the track-aligned variation and the limitations of a box-based method led us to take the following path:

i) Take the stellar count rates, determined as in Section 3.2 but without the pre-launch flatfield corrections applied, from individual science images for all usable stars within 512 bins of the CCD centre.
ii) Take the ratio of each count rate to the predicted count rate with the previously derived correction factors to instrument response applied.
iii) Treat the data as a single set of values of ratio against pixel coordinates.
iv) Fit a suitable functional form, using the L1 norm and weighting all the measurements for each star by its interquartile range.

Using the results from the box-based analysis and the pre-launch flatfield from Section 2.2 (Equation (3)) as a guide, we tried a form

$$FF(r) = a_0 + a_1 R^2 + a_2 R^4 + a_3 \max(R - a_4, 0)^2, \tag{11}$$

where R is the radial distance from the image centre. For HI-2A, the results are tabulated in Table 5. We were not able to obtain a useful fit for HI-2B as too few stars were sufficiently well-behaved across the whole field of view, but the results appear to be consistent with those for HI-2A. The addition of non-radial terms to the relation did not give any measurable improvement in the fit, so we consider that the form given in Equation (11) with the coefficients derived for HI-2A and listed in Table 5 represents the best large-scale flatfield that we can obtain for both HI-2 cameras.
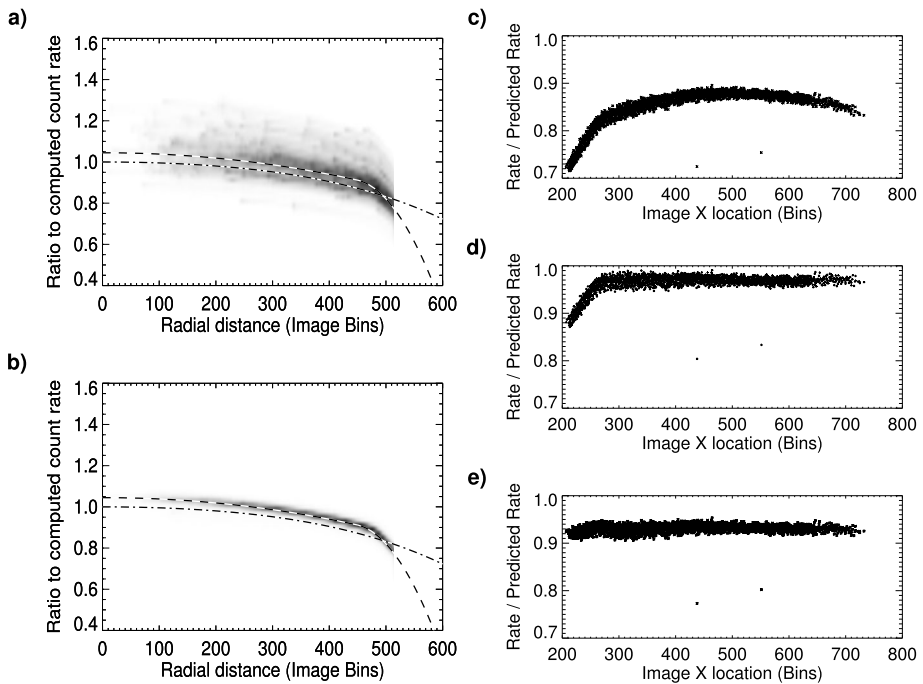
Figure 10 The corrected large-scale flatfield for HI-2A. (a) Compared with the raw ratios of the count rate to that predicted at field centre. The greyscale map is a 2D histogram of the measurements, the dash–dot curve is the pre-launch flatfield, and the dashed curve is the fit presented here. (b) Compared with the same ratios, but normalised on a source-by-source basis. The format is the same as for (a). (c – e) Comparison of the counting rate for the star η Norma (G8III, $m_v = 4.65$) as it tracks across the CCD. (c) The raw ratio, (d) corrected with the pre-launch flatfield, (e) corrected with the new flatfield.

In Figure 10a we show a 2D histogram of the ratios of the measured count rate to that predicted as a function of radial distance from the CCD centre. This clearly shows that the shape of the fit is at least consistent with the histogram, but there is a large scatter. The structure of the histogram strongly suggests the scatter to be mainly due to variations from star to star. As with the instrument degradation analysis (Section 5), we therefore rescaled each star so that its median ratio after applying the flatfield was 1.0, and then regenerated the histogram. This revised histogram is shown in Figure 10b, which shows that the shape of the revised fit is indeed an excellent fit to the data. We also show (Figure 10c – e) the effect of the flatfield correction on an individual star, in this case η Norma, which shows that the corrected stellar count rate is constant across the CCD with the revised flatfield.

The revised flatfield was added to secchi_prep on 1 July 2015 along with the revised conversion coefficients.

7. Summary

We may summarise the results obtained in this study as follows:

i) There are small but significant corrections to be made to the photometric calibration parameters of the two HI-2 instruments, the correction factors are 1.043 for HI-2A and

0.946 for HI-2B with both being accurate to about 2 %. The SolarSoft processing routines were updated to use these revised parameters on 1 July 2015.

ii) The stability of the photometric sensitivity of the HI-2 cameras (like the HI-1 cameras) through the mission is very good. HI-2A is degrading at about 0.16 % year^{-1} and HI-2B at about 0.07 % year^{-1}, which is about an order of magnitude slower than for other white-light imaging instruments.

iii) The large-scale flatfield must be modified to account for substantial vignetting in the outer parts of the field of view beyond about 450 image bins from the CCD centre. There is no need to introduce non-axisymmetric terms.

iv) The lack of dependency of the photometric corrections on spectral type suggests that the pre-launch bandpass determinations are accurate.

v) The detectors appear to be linear up to the onset of saturation. Saturation is not a factor for heliospheric use of the HI-2 instruments, but must be taken into account for stellar observations.

vi) The AZP projection is not a perfect representation of the HI-2 projection, but the errors from its use are small compared with other uncertainties in CME measurements.

Appendix A: Magnitude Scales

In this appendix we describe the steps required to compute the predicted count rates for stars, given their spectral types and V-magnitudes.

A.1 Calibrating the Spectra

The spectra given by Pickles (1998) are all normalised to a value of 1.0 at 555.6 nm. Gray (2005) gives the following equation to relate the physical flux at 555.6 nm to V-band magnitude [m_v]:

$$\log F_{555.6} = -0.4 m_v - 10.449 \ \mathrm{W\,m^{-2}\,nm^{-1}}. \tag{12}$$

However, this is exact only for A0V types, and it holds only approximately for other spectral types (the relation is accurate to about 10 % apart from late-M class stars). To obtain more accurate conversions, we use a numerical integration of the spectrum multiplied by the V-band profile to determine physical units. The improved conversion factors are illustrated in Figure 11.

Figure 11 The flux density of different spectral types of star at $\lambda = 555.6$ nm for $m_v = 0.0$. Solid = main sequence, dashed = supergiants, and dash–dot = giants. The horizontal dotted line is the value from Equation (12).
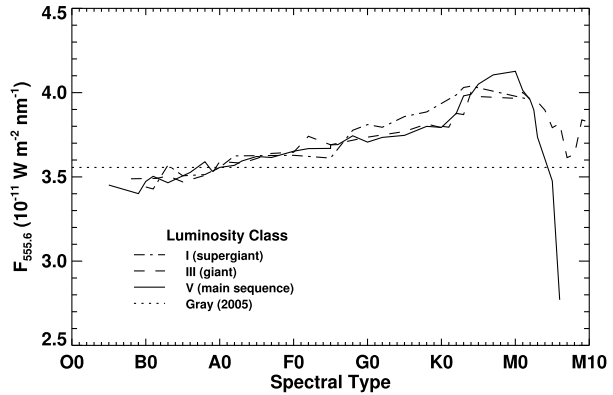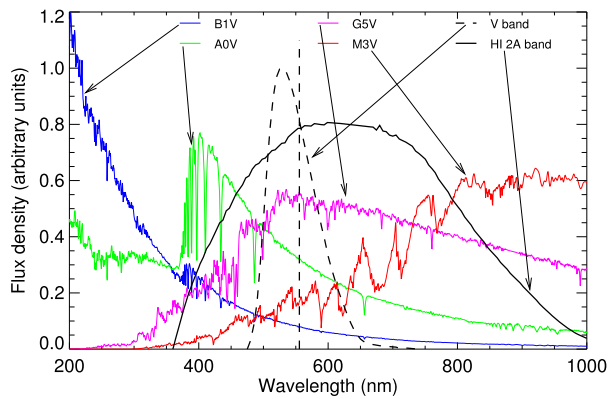

Figure 12 The spectra of various main-sequence types compared with the V and HI-2A passbands. The vertical dashed line indicates a wavelength of 555.6 nm. N.B. the scaling of the spectra is arbitrary and designed to make them all visible.

A.2 HI-2 Magnitudes

As we explained in Section 2.1, the HI-2 responses are much broader-band than those of HI-1 (Figure 1b and Article 1) as the optics do not have a filter coating. The resulting pass-band is also much broader than the V-band used for most catalogue magnitudes (the region of sensitivity spans the B, V, R, and I bands). Because of this, stars of different spectral types and the same V magnitude may have very different intensities in the HI-2 passbands (Figure 12). We therefore define a HI-2 magnitude such that

$$m_{\mathrm{hi2}} = -2.5 \log_{10} \left(\frac{\int_0^\infty F(\lambda) T_{\mathrm{hi2}}(\lambda) \, \mathrm{d}\lambda}{\int_0^\infty F_0(\lambda) T_{\mathrm{hi2}}(\lambda) \, \mathrm{d}\lambda} \right), \tag{13}$$

where $F(\lambda)$ is the spectral flux density of the star and $F_0(\lambda)$ is the spectral flux density of a star of type A0V, and $m_v = 0$; T_{hi2} is the passband of the HI-2 instrument under consideration. For any spectral type, a HI-2 magnitude correction may be determined by evaluating Equation (13) for an $m_v = 0$ spectrum for that type.

Because the HI-2 instruments (as for any CCD-based detectors) are photon counters and not bolometric detectors, the HI-2 magnitude will not give a measure of the apparent brightness of a star in the HI-2 field of view; a redder star will appear brighter as more photons are needed to produce the same flux at longer wavelengths. It is, therefore, also
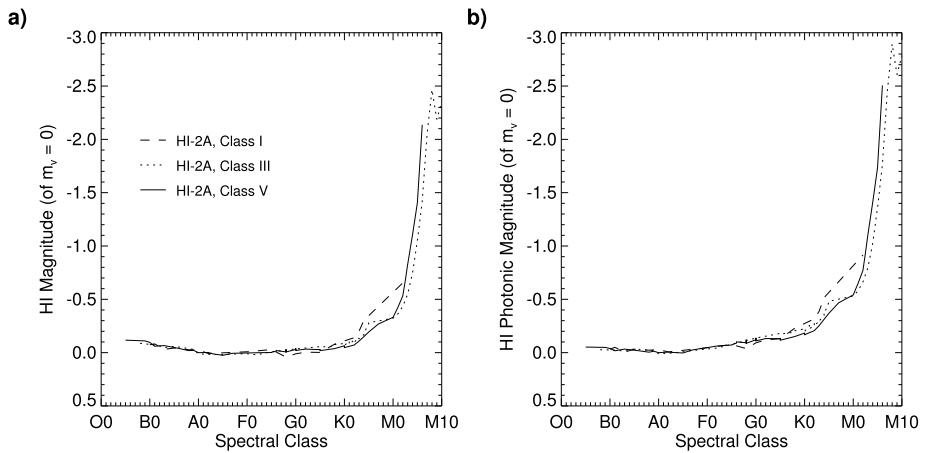
Figure 13 Relation between HI-2A magnitudes and the visual magnitude scale for luminosity classes I (super giants), III (giants), and V (main sequence). (a) Regular magnitude and (b) photonic magnitude. The curves for HI-2B are very similar.

useful to define a photonic magnitude that indicates the V-magnitude of an A0V star that would appear to have the same brightness in the HI-2 detectors. This is defined as

$$\mu_{\text{hi2}} = -2.5 \log_{10} \left(\frac{\int_0^\infty F(\lambda) T_{\text{hi2}}(\lambda) \frac{\lambda}{hc} \, d\lambda}{\int_0^\infty F_0(\lambda) T_{\text{hi2}}(\lambda) \frac{\lambda}{hc} \, d\lambda} \right), \tag{14}$$

with a correction being defined in the same manner as for the HI-2 magnitude. This photonic magnitude is used in defining the magnitude limits of the calibration sample.

The relation between the HI magnitudes and photonic magnitudes and the visual magnitude scale for HI-2A is summarised in Figure 13. A more detailed summary is provided in the supplemental file M0_summary.csv (the contents of the columns are described in the file README.ME), which tabulates the properties of $m_v = 0$ stars as observed by both of the HI-2 instruments.

Appendix B: Saturation and Non-linearity

In the HI detectors, saturation is a non-trivial phenomenon because the images are binned and summed onboard the spacecraft before being transmitted to Earth. As a result of this, there is expected to be a gradual onset of saturation, which is not easy to distinguish from non-linearity in the detector system. Fortunately, this can be investigated because approximately once a day, a single-exposure unbinned image is transmitted. These images are in units of DN with the only correction being the subtraction of the bias level.

To investigate any possible non-linearity, we took all of the stars from our sample passing within 300 CCD pixels of the image centre and plotted the brightness of the highest pixel in the stars as a function of their HI-2A photonic magnitudes (Appendix A). The results are shown in Figure 14. It is clear that there is a cutoff for HI-2A at about magnitude 4.3, at which point the peak counts reach a maximum. Below this level, the response does not deviate significantly from linearity. For HI-2B, where the peak count rate is lower for a given brightness due to the large PSF, the behaviour is similar, although the cutoff is not
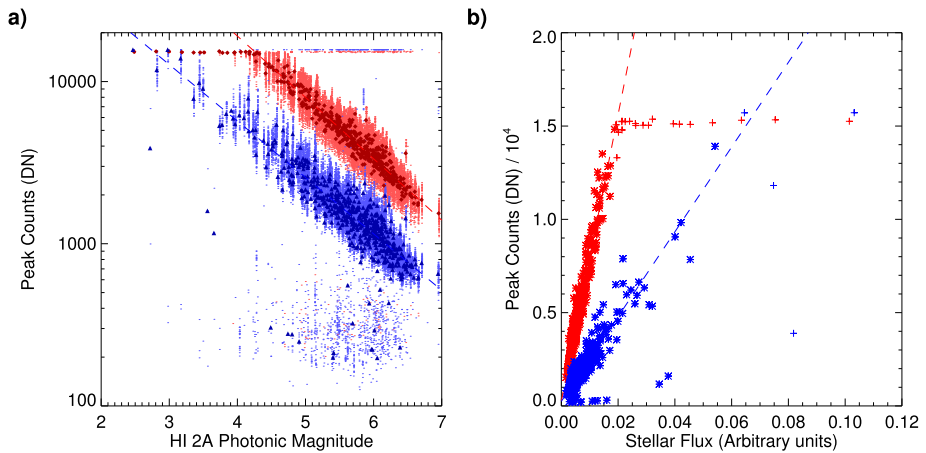
Figure 14 The peak counts of stars as a function of brightness. (a) All of the measurements as a function of photonic magnitude, HI-2A is the upper group of points, shown in red, HI-2B is the lower group of points, shown in blue. (b) The medians for each star as a function of brightness, along with fits to the points below the apparent cut-off levels. In (b) points below the cutoff are marked by asterisks, those above by plus signs.

as well defined and appears to be at about magnitude 3. The maximum counts observed are about 15650 DN for HI-2A and 15710 DN for HI-2B, which is equal to the maximum value that the 14-bit A-to-D converter can record ($2^{14} - 1$ DN) minus the DC bias levels of about 735 DN for HI-2A and 675 DN for HI-2B. This implies that the limit of the A-to-D converter is below the full-well level of the CCD.

Since the peak level due to the $F + K$ coronal brightness is only about 2000 DN in a single exposure in the region of the HI-2 fields closest to the Sun, there is no need to apply any non-linear corrections to the instrumental conversion factors or to be concerned about saturation for heliophysics investigations. However, the effects of partial saturation must be taken into account when using the HI-2 instruments for stellar work such as variable star or bright nova studies. A detailed study of the way in which measurements of bright stars are affected by saturation is beyond the scope of this analysis.

Appendix C: Derivation of the Diffuse Correction

In this appendix we present a derivation of the geometrical correction to the flux-conversion factors for extended sources, the results of which were quoted in Section 4.2.2.

As we stated there, the projection of the HI instruments is well approximated by the AZP projection (Equation (9)):

$$R = \frac{F_p(\mu + 1)\sin\alpha}{\mu + \cos\alpha}.$$

This projection is represented by the geometrical construction in Figure 15a (unlike the figures in Calabretta and Greisen (2002) and Brown, Bewsher, and Eyles (2009), we have shown a value of μ between 0 and 1, which is the situation for the HI projections).

To compute the diffuse correction, we need to determine the area of sky (or globe) that will be projected onto a defined region of the image plane (for convenience we refer to the region as a pixel). Since the AZP projection is circularly symmetrical, we do not need to
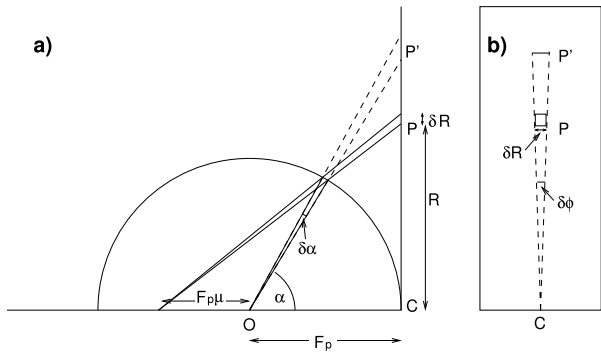
consider the azimuthal position of the pixel on the CCD, only its distance from the CCD
centre and its size. Let that pixel be at the point P (Figure 15) a distance R from the field
centre and be square with a linear size δR. This pixel observes a region of the sky at an angle
α from the optical axis. Let P' also be the location of the projection of the area of sky seen
by the pixel onto the image plane from the centre of the sphere $[O]$, *i.e.* where that area of
sky would be projected in the tan projection (Brown, Bewsher, and Eyles, 2009; Thompson
and Wei, 2010). The angle subtended on the sky by that pixel (which is assumed to be small)
in the α-direction is given by

$$\delta\alpha = \delta R \frac{d\alpha}{dR} = \delta R \Big/ \frac{dR}{d\alpha} = \frac{\delta R}{F_p(\mu+1)} \frac{(\mu + \cos\alpha)^2}{\mu\cos\alpha + 1}. \tag{15}$$

In the image plane (Figure 15b), the pixel subtends an angle $\delta\phi = \delta R/R$ at the inter-
section of the optical axis and the image plane $[C]$. Its angular size on the sky $[\delta\phi']$ is
the angular size of a line segment at P' subtending $\delta\phi$ at C, as seen from O. From basic
trigonometry $\frac{CP'}{OP'} = \sin\alpha$, so that (in the small-angle approximation) the angular size of the
pixel perpendicular to the plane of Figure 15 is given by

$$\delta\phi' = \delta\phi\sin\alpha = \frac{\delta R\sin\alpha}{R} = \delta R\frac{\mu + \cos\alpha}{F_p(\mu+1)}. \tag{16}$$

Since both $\delta\alpha$ and $\delta\phi'$ are small angles, we may determine the solid angle subtended by the
pixel on the sky by using $\delta\Omega = \delta\phi'\delta\alpha$, *i.e.*

$$\delta\Omega = \left(\frac{\delta R}{F_p(\mu+1)}\right)^2 \frac{(\mu + \cos\alpha)^3}{\mu\cos\alpha + 1}. \tag{17}$$

We may thus define a correction factor $[\rho]$ by which the raw image must be divided to
correct for pixel projected area as

$$\rho = \frac{\delta\Omega(\alpha)}{\delta\Omega(0)} = \frac{(\mu + \cos\alpha)^3}{(\mu+1)^2(\mu\cos\alpha + 1)}. \tag{18}$$

Since the quantity that we measure directly is the distance from the CCD centre rather than
the sky angle, it is then useful to invert the AZP projection of Equation (9), which can be
relatively readily done as follows: let $\gamma = F_P(\mu+1)/R$, and rearrange to give

$$\mu + \cos\alpha = \gamma\sin\alpha,$$

square both sides and recall that $\sin^2\alpha = 1 - \cos^2\alpha$:

$$\mu^2 + 2\mu\cos\alpha + \cos^2\alpha = \gamma^2\big(1 - \cos^2\alpha\big),$$

or

$$\left(1 + \gamma^2\right)\cos^2\alpha + 2\mu\cos\alpha + \left(\mu^2 - \gamma^2\right) = 0.$$

This can be solved to give

$$\cos\alpha = \frac{-\mu \pm \gamma\sqrt{1 - \mu^2 + \gamma^2}}{1 + \gamma^2}. \tag{19}$$

The positive value for the discriminant is the one appropriate to obtain values of $\alpha < 90°$. This is a more convenient formulation for our purposes than that given by Calabretta and Greisen (2002) since we need $\cos\alpha$ rather than α.

Appendix D: Deviations from AZP

Throughout the analyses presented in the main body of this article, we have followed Brown, Bewsher, and Eyles (2009) and assumed that the AZP projection (Equation (9)) is an accurate representation of the actual projection of the HI-2 instruments. This is a purely empirical association, however; the HI optics were not designed so as to yield an AZP projection. Therefore in this appendix we describe some checks on the accuracy of that assumption as applied to HI-2.

To determine this, we measured the location of each star brighter than $m_v = 5.0$ in the Yale catalogue (Hoffleit and Warren, 1995) in the first image of the first, sixth, *etc.* day of each month throughout the mission using an interpolated maximum pixel location, *i.e.*

$$x = \frac{\sum_{i=-1}^{1}((m + i)I_{m+i,n}^2)}{\sum_{i=-1}^{1} I_{m+i,n}^2};$$

$$y = \frac{\sum_{j=-1}^{1}((n + j)I_{m,n+j}^2)}{\sum_{j=-1}^{1} I_{m,n+j}^2}.$$

Here (m, n) is the location of the local maximum and I is the counting rate in the image. We found that the dominant effect is a radial distortion, which is shown in Figure 16.

The general trends are very similar in the two instruments, and in each case the median displacement at any radial distance within the 512-bin radius field of view of the HI-2 cameras is less than 0.5 image bins (1 CCD pixel). Beyond that, in the corners of the CCD the deviation becomes considerably larger, exceeding 4.0 bins by the extreme edge of detection. The shape of the variation shows that the true projection must be at least a three-parameter relation, and so the distortion cannot be corrected by simply adjusting the AZP parameters.

It is possible to achieve an improved match by fitting the AZP parameters in only the inner part of the field of view and then adding a power-law correction in the outer parts to change Equation (9) into

$$R = \frac{F(\mu + 1)\sin\alpha}{\mu + \cos\alpha} + D\max(\alpha - \alpha_D, 0)^4,$$

where D is a coefficient quantifying the deviation from AZP and α_D is the angle beyond which deviation from AZP starts. However, even this fails in the corners of the field of view (beyond 512 bins from the centre of the CCD). Therefore, since the errors incurred in position determination by using the AZP projection are small compared with the size of the HI-2 PSFs and the accuracy with which a CME can be located, we consider that the improved accuracy does not justify the additional algebraic complexity. It is also noted
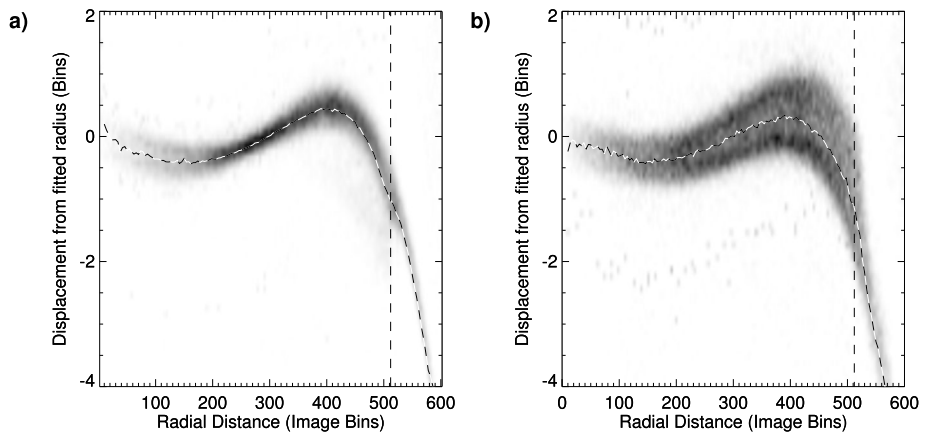
Figure 16 The radial deviation of the actual HI-2 projections from the AZP projection that has been assumed. (a) HI-2A and (b) HI-2B. In both cases the greyscale plot shows a 2D histogram of the displacements of stars brighter than magnitude 5.0, and the overlaid trace shows the median displacement. The vertical dashed line indicates the edge of the circular field of view.

that the implied corrections to the off-axis diffuse correction (Section 4.2.2) are smaller than 1 %. For stellar analyses, the deviations are significant, but they are not large enough to cause mis-identification of stars.

The double-peaked nature of the HI-2B histogram (Figure 16b) has its origin in a slight distortion that has the shape of a banana, where objects well North and South of the CCD centre are displaced slightly East of the AZP predicted position. It seems probable that this originates from the same manufacturing issue that affected the focusing of HI-2B (Eyles *et al.*, 2009).

References

Allen, C.W.: 1976, *Astrophysical Quantities*, 3rd edn. Athlone Press, London.

BenMoussa, A., Gissot, S., Schühle, U., Del Zanna, G., Auchère, F., Mekaoui, S., Jones, A.R., Walton, D., Eyles, C.J., Thuillier, G., Seaton, D., Dammasch, I.E., Cessateur, G., Meftah, M., Andretta, V., Berghmans, D., Bewsher, D., Bolsée, D., Bradley, L., Brown, D.S., Chamberlin, P.C., Dewitte, S., Didkovsky, L.V., Dominique, M., Eparvier, F.G., Foujols, T., Gillotay, D., Giordanengo, B., Halain, J.P., Hock, R.A., Irbah, A., Jeppesen, C., Judge, D.L., Kretzschmar, M., McMullin, D.R., Nicula, B., Schmutz, W., Ucker, G., Wieman, S., Woodraska, D., Woods, T.N.: 2013, *Solar Phys.* **288**, 389. ADS. DOI.

Bewsher, D., Brown, D.S., Eyles, C.J.: 2012, *Solar Phys.* **276**, 491. ADS. DOI.

Bewsher, D., Brown, D.S., Eyles, C.J., Kellet, B.J., White, G.J., Swinyard, B.: 2010, *Solar Phys.* **264**, 433. ADS. DOI.

Branham, R.L.: 1982, *Astron. J.* **87**, 928. ADS. DOI.

Brown, D.S., Bewsher, D., Eyles, C.J.: 2009, *Solar Phys.* **254**, 185. ADS. DOI.

Buffington, A., Morrill, J.S., Hick, P.P., Howard, R.A., Jackson, B.V., Webb, D.F.: 2007, *SPIE* **CS–6689**, 66890B. ADS. DOI.

Calabretta, M.R., Greisen, E.W.: 2002, *Astron. Astrophys.* **395**, 1077. ADS. DOI.

Eyles, C.J., Harrison, R.A., Davis, C.J., Waltham, N.R., Shaughnessy, B.M., Mapson-Menard, H.C.A., Bewsher, D., Crothers, S.R., Davies, J.A., Simnett, G.M., Howard, R.A., Moses, J.D., Newmark, J.S., Socker, D.G., Halain, J.-P., Defise, J.-M., Mazy, E., Rochus, P.: 2009, *Solar Phys.* **254**, 387. ADS. DOI.

Gonzalez, R.C., Woods, R.E.: 2008, *Digital Image Processing*, 3rd edn. Pearson Education, Upper Saddle River (Chapter 9).

Gray, D.F.: 2005, *The Observation and Analysis of Stellar Photospheres*, 3rd edn. Cambridge University Press, Cambridge, 211.

Hoffleit, D., Warren, W.H. Jr.: 1995, *VizieR Online Data Catalog* **5050**. vizier.cfa.harvard.edu/viz-bin/VizieR?-source=V/50. ADS.

Howard, R.A., Moses, J.D., Vourlidas, A., Newmark, J.S., Socker, D.G., Plunkett, S.P., Korendyke, C.M., Cook, J.W., Hurley, A., Davila, J.M., Thompson, W.T., St. Cyr, O.C., Mentzell, E., Mehalick, K., Lemen, J.R., Wuelser, J.P., Duncan, D.W., Tarbell, T.D., Wolfson, C.J., Moore, A., Harrison, R.A., Waltham, N.R., Lang, J., Davis, C.J., Eyles, C.J., Mapson-Menard, H., Simnett, G.M., Halain, J.P., Defise, J.M., Mazy, E., Rochus, P., Mercier, R., Ravet, M.F., Delmotte, F., Auchere, F., Delaboudinière, J.P., Bothmer, V., Deutsch, W., Wang, D., Rich, N., Cooper, S., Stephens, V., Maahs, G., Baugh, R., McMullin, D., Carter, T.: 2008, *Space Sci. Rev.* **136**, 67. ADS. DOI.

Kaiser, M.L., Kucera, T.A., Davila, J.M., St. Cyr, O.C., Guhathakurta, M., Christian, E.: 2008, *Space Sci. Rev.* **136**, 5. ADS. DOI.

Koenker, R., Hallock, K.F.: 2001, *J. Econ. Perspect.* **15**, 143.

Kopp, G., Lean, J.L.: 2011, *Geophys. Res. Lett.* **38**, L01706. ADS. DOI.

Kurucz, R.L., Furenlid, I., Brault, J., Testerman, L.: 1984 In: *National Solar Observatory Atlas No. 1 Solar Flux Atlas from 296 to 1300 nm*, National Solar Observatory, Tuscon. ADS.

Llebaria, A., Lamy, P., Danjard, J.-F.: 2006, *Icarus* **182**, 281. ADS. DOI.

Neckel, H., Labs, D.: 1984, *Solar Phys.* **90**, 205. ADS. DOI.

Pickles, A.J.: 1998, *Publ. Astron. Soc. Pac.* **110**, 863. ADS. DOI.

Scheuer, P.A.G.: 1957, *Proc. Camb. Phil. Soc.* **53**, 764. ADS. DOI.

Thernisien, A.F., Morrill, J.S., Howard, R.A., Wang, D.: 2006, *Solar Phys.* **233**, 155. ADS. DOI.

Thompson, W.T., Wei, K.: 2010, *Solar Phys.* **261**, 215. ADS. DOI.

Wall, J.V.: 1979, *Q. J. Roy. Astron. Soc.* **20**, 138. ADS.

Wall, J.V.: 1996, *Q. J. Roy. Astron. Soc.* **37**, 519. ADS.

Zacharias, N., Monet, D.G., Levine, S.E., Urban, S.E., Gaume, R., Wycoff, G.L.: 2004, *Bull. Am. Astron. Soc.* **36**, 1418. ADS.